

High temporal resolution SO₂ flux measurements at Erebus volcano, Antarctica

Marie Boichu^a, Clive Oppenheimer^a, Vitchko Tsanev^a, Philip R. Kyle^b

^a*Department of Geography, University of Cambridge, Downing Place, Cambridge CB2 3EN, United Kingdom*

^b*Department of Earth and Environmental Science, New Mexico Institute of Mining and Technology, Socorro, NM 87801, USA*

Abstract

The measurement of SO₂ flux from volcanoes is of major importance for monitoring and hazard assessment purposes, and for evaluation of the environmental impact of volcanic emissions. We propose here a novel technique for accurate and high time resolution estimations of the gas flux. We use two wide field of view UV spectrometers capable of collecting, instantaneously, light from thin parallel cross sections of the whole gas plume, obviating the need for either traversing, scanning or imaging. It enables tracking of inhomogeneities in the gas cloud from which accurate evaluation of the plume velocity can be made by correlation analysis. The method has been successfully applied on Mt. Erebus volcano (Antarctica). It yields estimations of the plume velocity and gas flux at unprecedented time resolution (1 Hz) and high accuracy (uncertainty of 33%). During a ~ 2 h experiment on 26 December 2006, SO₂ flux varied between 0.17 and 0.89 ± 0.2 kg s⁻¹ with a vertical plume velocity varying between 1 and 2.5 ± 0.1 m s⁻¹. These

Email addresses: mb632@cam.ac.uk (Marie Boichu), co200@cam.ac.uk (Clive Oppenheimer), vip20@cam.ac.uk (Vitchko Tsanev), kyle@nmt.edu (Philip R. Kyle)

Preprint submitted to Journal of Volcanological and Geothermal Research November 30, 2009

measurements provide insight into the short-term variations of the passive degassing of this volcano renowned for its active lava lake. A cyclicity in flux, ranging from about 11-24 min, is evident. We propose two physical mechanisms to explain this degassing pattern, associated to periodic supply of either gas-rich magma or gas alone into the lake. The dual-wide field of view DOAS technique promises better integration of geochemical and geophysical observations and new insights into gas and magma dynamics, as well as processes of magma storage and gas segregation at active volcanoes.

Key words: Volcanic degassing, DOAS spectroscopy, high time resolution gas flux

1. Introduction

Gas emissions from volcanoes are measured for several purposes, including monitoring, hazard assessment, and investigation of environmental impact. For over a century, fumarole chemistry has been studied using in-situ collection techniques. While these yield highly detailed analysis of fluid composition, field access can be limited and data streams are often discontinuous. However, since the first application of the correlation spectrometers (COSPEC), four decades ago (Moffat and Millan, 1971; Stoiber and Jepsen, 1973), numerous ground-based, airborne and spaceborne optical remote sensing instruments and methods have emerged capable of measuring both volcanic gas fluxes and composition, for individual vents or an entire plume, and with improved temporal resolution (McGonigle and Oppenheimer, 2003). As a result, gas geochemistry has increasingly found its place among the operational techniques of volcano monitoring (Oppenheimer, 2003; Galle et al.,

2003). Nevertheless, the time resolution of gas measurements still lags behind what is routinely achieved in geophysical studies, limiting progress in understanding the links between seismicity, deformation and degassing that are clearly of considerable relevance for understanding volcano behavior, especially the transition to explosive activity (Fischer et al., 1994; Watson et al., 2000; Young et al., 2003). Some volcanoes clearly exhibit rapid changes in gas composition and flux related to magmatic activity. For instance, Oppenheimer et al. (2006) and Burton et al. (2007) have demonstrated pronounced compositional differences in gas emissions associated with and between Strombolian eruptions using the technique of open-path Fourier transform infrared spectroscopy. This technique enables observations at a frequency of about 1 Hz. But achieving comparable time resolution for gas flux measurements is another challenge, since the entire plume needs to be captured.

The most widespread method used for measuring volcanic gas fluxes is scattered light ultraviolet spectroscopy (see e.g. McGonigle and Oppenheimer (2003) for a review) using correlation spectroscopy or Differential Optical Absorption Spectroscopy (DOAS). The plume is usually profiled across its transport direction from below with a zenith-viewing telescope, the apparatus being mounted on a moving vehicle, or by use of a scanning system (Fischer et al., 2002; Edmonds et al., 2003). The flux is then obtained from the product of the gas column abundance (integrated across the plume section) and the plume transport speed. The main sources of uncertainty in flux measurements made in this way are generally considered to be linked

40 to light scattering processes (Millan, 1980; Mori et al., 2006; Kern et al.,
 41 2009) and to the error in the plume speed estimation (Stoiber et al., 1983;
 42 Williams-Jones et al., 2006), which is sometimes taken to be the wind speed
 43 measured or modelled close to the plume altitude. But even if wind speed is
 44 measured at the exact plume altitude, it may not represent well the plume
 45 velocity due to the complex wind-fields that develop downwind of volcanoes
 46 due to topography. Different methods have been proposed to enhance plume
 47 speed accuracies but are not yet widely used. One approach is to use mul-
 48 tiple UV spectrometers sited at fixed positions some distance apart so as to
 49 track the transport of inhomogeneities in the plume (McGonigle et al., 2005a;
 50 Williams-Jones et al., 2006); related approaches use a single instrument car-
 51 ried beneath the plume, with optics that enable alternating fields of view,
 52 one at zenith, the other inclined (McGonigle et al., 2005b), or simultane-
 53 ous measurements in two directions using a double spectrometer (Johansson
 54 et al., 2009). Latterly, imaging UV techniques (imaging DOAS or UV cam-
 55 eras combined with appropriate narrow band filters) have been demonstrated
 56 (Bobrowski et al., 2006; Bluth et al., 2007; Mori and Burton, 2006), which
 57 can achieve a high time resolution on flux measurements.

58

59 Here we propose an alternative, simple solution which is to use a system
 60 employing two UV spectrometers equipped with wide field of view telescopes
 61 that instantaneously collect light from two narrow and parallel entire cross
 62 sections of the plume (Fig. 1). This obviates the need for either traversing,
 63 scanning or imaging. We will use the acronym DW-FOV DOAS (dual wide
 64 field of view DOAS) to refer to this technique. By using two spectrometers

65 with fields of view separated by a small angle, time-series of retrieved gas
66 amounts can be correlated to obtain (through knowledge of the viewing and
67 plume geometry) the plume transport speed through time. Such a system
68 is capable, therefore, of accurate, highly time-resolved measurements of vol-
69 canic gas fluxes.

70

71 The aim of this paper is to describe this new instrumentation and method-
72 ology, and to apply the approach to rapid measurements of SO₂ fluxes at Mt.
73 Erebus in Antarctica. Interest in the emissions from Erebus is fuelled by the
74 potential impact of sulfur, halogens and NO_x on the pristine atmospheric en-
75 vironment (Radke, 1982; Zreda-Gostynska et al., 1993, 1997; Oppenheimer
76 et al., 2005, 2009a), but also because the volcano is renowned for its dynamic
77 lava lake and Strombolian activity. This technique provides new possibili-
78 ties to investigate the magma degassing of volcanoes that exhibit short-term
79 variability in the dynamics of magma transport and degassing, which are
80 reflected in changes in eruptive behavior (Oppenheimer et al., 2009b; Harris
81 et al., 2005). Measurements are now also much more comparable in terms
82 of frequency of data acquisition with observations provided by common geo-
83 physical tools such as seismology. At Erebus, interpretation of the observed
84 SO₂ variations in terms of magma dynamics is simplified by the limited role
85 of hydrothermal scrubbing of emissions (Symonds et al., 2001). Moreover,
86 observations of SO₂ flux from the volcano by scanning UV spectroscopy have
87 previously suggested a periodicity of ~ 10 min (Sweeney et al., 2008), which
88 we are keen to investigate further.

89 After a section describing the methodology, we will present the high res-

olution time-series of plume speed and flux obtained at Erebus. A wavelet analysis of these flux observations reveal distinctive patterns in degassing. We will discuss about their interpretation in terms of gas and magma dynamics as well as processes of magma storage and gas sequestration. Finally, three appendixes include some technical content and an electronic supplement to this article presents an animation showing the results in form of a "SO₂ fluxmeter" superimposed on video of the plume.

2. Methodology

Note that all mathematical symbols used in the following are listed in Table 1.

2.1. Experiment description

We collected UV DOAS spectroscopic measurements at Erebus on the 26 December 2006 during conditions of clear sky and low wind, such that the plume rose approximately vertically from the crater. Spectra were recorded using two Ocean Optics USB4000 spectrometers spanning a wavelength range of about 283–440 nm, with a resolution of, respectively, 0.5 and 0.6 nm (FWHM). Hoya filters were used to reduce the amount of stray light. As shown in Fig. 1, each spectrometer was attached to a telescope consisting of spherical and cylindrical lenses that provide a horizontal angle of aperture θ_{WFOV} of $\sim 22^\circ$, giving an elongated horizontal field of view, and a narrow vertical angle of aperture θ_{NFOV} of $\sim 0.5^\circ$ defined by the width of the spectrometer's slit and the focal length of the positive lens. The long axis of the field of view (d_X) was designed so that the projected θ_{WFOV} footprint (equivalent to ~ 810 m at the distance of the plume of ~ 2004 m here) would

114 sample the entire plume. The long axes of the fields of view were parallel
 115 but displaced, so that each instrument viewed a different cross-section of the
 116 plume, determined by the observation geometry.

117

118 Spectra from each instrument were recorded on to separate laptop com-
 119 puters, whose clocks were synchronized using a GPS unit so as to yield a
 120 time-stamped series of data. All observations were made from Lower Erebus
 121 Hut, a horizontal distance D of ~ 1960 m from the summit of Erebus, and
 122 mostly viewed the vertically-rising plume during periods with very low winds.
 123 The elevation of the lowermost field of view (α) was $\sim 12^\circ$ and separation of
 124 the two fields of view (β) was 2.0° , precisely adjusted thanks to a goniometer.
 125 The distance d_Y between the two fields of view is then:

$$d_Y = D \left[\tan \left(\frac{\pi}{180} (\alpha + \beta) \right) - \tan \left(\frac{\pi}{180} \alpha \right) \right] \quad (2.1)$$

126

127 and was equal to ~ 72 m at the summit. The plume was thus crossed
 128 at respectively ~ 78 and ~ 150 m above the crater. Spectra were collected
 129 with an exposure time of 130 ms, maximizing their amplitude but avoiding
 130 saturation below 350 nm, and 8 spectra were averaged resulting in a time-
 131 step of ~ 1 s between measurements. 'Background' and 'dark' spectra were
 132 recorded at the start of each set of observations. Background spectra were
 133 collected by rotating both spectrometers about the vertical axis so as to point
 134 out of the plume.

135 2.2. Spectroscopic retrieval

136 SO₂ column amounts were retrieved following differential optical absorp-
137 tion spectroscopy (DOAS) procedures (Platt and Stutz, 2008). The reference
138 spectra included in the nonlinear fit were obtained by using Windoas convolv-
139 ing high-resolution SO₂ (293K, air) (Bogumil et al., 2003) and O₃ (246K, air)
140 (Burrows et al., 1999) cross-sections with Gaussian instrumental line shapes
141 estimated using a mercury lamp (FWHM = 0.5 and 0.6 nm for the lower
142 and upper spectrometers, respectively). A Ring spectrum calculated using
143 DOASIS was also included in the fit as well as a third order polynomial to
144 remove broad band structures from measured optical densities. The same op-
145 timized fitting window (307.6–330.0 nm) was selected to analyze data from
146 both spectrometers, yielding a near random fit residual structure with min-
147 imal standard deviation. As a result, the fit residual was between ten and
148 twenty times smaller than the SO₂ fit. Spectra recorded with the upper spec-
149 trometer are slightly noisier than those from the lower one leading to an error
150 of a few percent higher on the retrieved column amounts. The obtained time
151 series of the SO₂ column amounts for both instruments are shown in Fig. 2.

152 We are using wide field of view UV spectrometers capturing instanta-
153 neously the whole horizontal plume cross-section at two different altitudes.
154 Hence, the retrieved gas amount for one W-FOV DOAS instrument can be
155 approximated by the mean column amount along the different directions in-
156 side the wide angle of observation, as shown in Appendix A. The relative
157 error on this approximation (Eq. A.18) depends on plume optical densities
158 of the studied volcano. As illustrated by Fig. 8, this relative error is of a
159 few percent for a weak gas emitter like Erebus, and could reach in the worst

160 case up to 45% for a strong gas emitter like Kilauea volcano (assuming SO₂
161 column amounts up to 5×10^{18} molec.cm⁻²).

162 2.3. Plume speed retrieval

163 Inhomogeneities, induced by turbulence or variations in volcanic degassing
164 rate, give characteristic structures to the plume, which can be observable
165 through the time series of the gas column amounts obtained for each spec-
166 trometer. Correlation analysis is used to estimate the transport speed of
167 these structures, representative of the spatially averaged plume velocity over
168 the distance separating the fields of view of each spectrometer and of the
169 mean plume speed on the time window used for correlation.

170 2.3.1. Principle of the cross correlation analysis

171 Estimating the plume speed (with a time resolution of ~ 1 s) at time
172 t requires calculation of the cross correlation coefficients between segments
173 of the two column amount time series selected using a sliding window of a
174 given duration ΔT , centred respectively in t for the lower spectrometer and
175 in $(t + \tau)$ for the upper spectrometer, where τ is the time shift between
176 the two windows (see Fig. 4 for symbols). Cross correlation coefficients
177 $CCF(t, \tau, \Delta T)$ consequently depend on three variables.

178 The time lag τ_{lag} between the upper spectrometer signal and the lower
179 one, corresponding to the time for an inhomogeneity to travel from the first
180 to the second instrumental FOV, is *a priori* equal to the time shift, giving
181 the absolute maximum of the cross-correlation coefficients calculated at time
182 t , with τ varying in $[0: \Delta\tau: \tau_{max}]$ where $\Delta\tau$ represents the incremental time
183 step of the cross correlation (equal to 2 s here) and τ_{max} the maximum value

184 of τ associated with the minimum expected plume speed taken equal to 0.1
185 m s⁻¹.

186 Plume speed v is deduced from this time lag according to the relation:

$$v = \frac{d_Y}{\tau_{lag}}. \quad (2.2)$$

187 Because spectrometer's fields of view do not cross perpendicularly the
188 plume but are slightly inclined, the distance d_Y separating them at the en-
189 trance of the plume is a bit different than at its exit, depending on the plume
190 depth (less than 400 m at Erebus which is the crater size seen by pointing
191 from Lower Erebus Hut). This uncertainty on d_Y is taken into account in the
192 estimation of error on the speed, developed in the result section, by assuming
193 an uncertainty of ± 50 m on the horizontal distance D between spectrometers
194 and plume.

195 2.3.2. Influence of the correlation window length

196 As shown in Fig. 3a, estimated plume speeds depend on the length of
197 the sliding correlation window, compared with the time interval between two
198 structures in the degassing. Velocities are smoothed with a long window,
199 while a narrow window yields estimations closer to the instantaneous plume
200 speed. However, very low velocities obtained with the narrow window (close
201 to ~ 0.1 m s⁻¹) do not have a physical meaning but show the limit of the
202 correlation analysis and the need for a refinement of the method to remove
203 them. Indeed, recurrent structures can exist in the observed degassing and
204 lead to a periodicity in the cross correlation function, relative to the time-
205 shift, which is more pronounced with a narrow window (Fig. 4). In this case,
206 the speed estimated from the absolute maximum of the CCF coefficients,

207 over the range of τ values, can yield a match between a structure recorded
 208 at the first spectrometer, not with the time-delayed corresponding structure
 209 at the second instrument as desired, but with a translated structure result-
 210 ing from a consecutive inhomogeneity in the plume. An additional criterion
 211 is thus required to determine a relevant time-lag by selecting the first local
 212 maximum of the CCF function. Moreover, this maximum is retained only if
 213 it presents a significant amplitude above a given threshold, which needs to be
 214 determined. If these criteria are not fulfilled, velocity cannot be estimated.
 215 Note that the longer the window, the less likely this artifact will arise, given
 216 that secondary peaks are more flattened due to the larger number of points
 217 taken into account for the correlation calculation.

218

219 A threshold is imposed on the local maximum in the cross correlation
 220 function, which has to exceed 0.5 to be retained. Indeed, a threshold of 0.8
 221 removes irrelevant very low velocities of $\sim 0.1 \text{ m s}^{-1}$, but also some relevant
 222 output speed values. With these additional criteria (considering a threshold
 223 of 0.5), we mainly observe velocities ranging from 1-2.5 m s^{-1} , with values
 224 very similar for both narrow and long windows (Fig. 3b). Estimates are not
 225 identical. Narrow window speeds are more dispersed because they represent
 226 near instantaneous velocities rather than the averaged ones obtained with the
 227 long window. Some limits of the correlation analysis using a narrow window,
 228 associated with characteristics of the gas plume, remain and explain large
 229 discrepancies with the speeds estimated using a long window. They lead to
 230 velocities mostly below 0.5 m s^{-1} or higher than 2.5 m s^{-1} . These limits in
 231 the method are explained in Appendix B.

232 3. Results

233 3.1. Time-series of SO_2 column amounts

234 SO_2 column amount time-series obtained for both spectrometers (Fig. 2)
235 reveal similar patterns, with a time delay expected for the upper instrument
236 dataset corresponding to the time for an inhomogeneity to travel from the
237 first to the second spectrometer FOV. The slight differences in amplitude
238 between the time-series can result from various processes.

239 The sensitivity of both instruments can be assumed to have a multiplica-
240 tive effect on the measured light intensity. Optical depths and gas column
241 amounts are consequently independent of it. On the other hand, the error
242 in the column amount from the DOAS retrieval, resulting from the fitting
243 procedure (Stutz and Platt, 1996; Hausmann et al., 1999), is between 3 and
244 12% for both instruments. It explains a part of these differences.

245 Additional errors in the column amount are linked to the scattering of
246 light by air molecules and particles (Millan, 1980; Platt et al., 1997; Mori
247 et al., 2006). The modelling work of Kern et al. (2009) gives a quantification
248 of this effect, including in-plume multiple scattering and the 'light dilution
249 effect'. Given the low SO_2 column amounts and aerosol load (with an aerosol
250 extinction coefficient assumed to be less than 0.5 km^{-1} , as at Etna (Fiorani
251 et al., 2009)), the very limited ash content in the Erebus plume, and the
252 distance ($\sim 2 \text{ km}$) between plume and spectrometers, the error on the esti-
253 mated column amount is less than 10% over the wavelength range used for
254 retrieval (308–330 nm). Nevertheless, the impact of the light dilution effect
255 may be underestimated with this study which does not consider a wide spec-
256 trometer angle of observation, especially when the plume is far from filling

257 the whole field of view. More experiments would be required to quantify
258 this phenomenon. Finally, light scattering influences the absolute amount of
259 gas but should have a negligible impact on the differences identified between
260 spectrometers because they are both pointing at about the same altitude,
261 equivalent to just 75 m apart when projected to the crater, leading to negli-
262 gible differences in light path lengths.

263 The plume studied in this experiment was mainly vertical. Contrary
264 to horizontal plumes, which are principally advected by the wind, vertical
265 plumes rise due to buoyancy. They can be influenced by the local wind field
266 at an altitude where their vertical buoyancy-induced velocity is smaller than
267 the horizontal component of the wind. At this stage, they expand laterally
268 forming a bend. If the two fields of view intersect such a bend, gas molecules
269 are effectively "counted" more than once, leading to an over-estimation of
270 the column amount. It can explain differences in column amount time-series,
271 the higher spectrometer being potentially the only one affected. We checked
272 video footage recorded during our experiment and observed occasionally a
273 bend in the plume at a height less than 200 m above the crater, i.e., below
274 the altitude of the upper spectrometer's FOV. It happened during three time
275 intervals (0-939,1464-1866,3354-3791 s after the start time of 20:24 h GMT),
276 and the column amounts measured with the upper instrument were only 2-
277 10% higher than those obtained with the lower spectrometer (see Fig. 2).
278 Consequently, this issue only weakly affects the results.

279 An additional process is associated with the presence of stagnant, dif-
280 fuse SO_2 around the plume, which sometimes forms a thin veil as seen on
281 the video. This background pollution is hard to quantify but is certainly

negligible compared with the previously mentioned processes.

Errors on column amounts (CA) are less than 10% for each spectrometer. The main differences between the two CA time-series are of higher magnitude and cannot be due to any of these artifacts but result from atmospheric phenomena to be discussed later. The lower field of view is likely to present the time variations in column amount the closest to those of the emission of gas at the magma source. It is consequently chosen for the flux estimation.

3.2. Plume speed time-series

We have seen in Section 2.3.2 some issues encountered when the plume speed is evaluated with a narrow correlation window (here of 2.5 min), due to limits of the correlation analysis method. When evaluations are available, estimated speeds are closer to real-time values, which is of considerable interest when studying very short-term eruptive behaviour such as explosions. There was no Strombolian activity during our experiment, and we are primarily interested in exploring periodic behaviour with cycles around 10 min. For this reason, the SO₂ flux is calculated from the speed estimated with a longer correlation window of 10 min (Fig. 5b). Cross correlation coefficients used for wind speed determination are shown in Fig. 5c with values most of the time significantly higher than the chosen threshold of 0.5. The average plume velocity varies smoothly over the range 1–2.5 m s⁻¹. By a basic differential calculation from Equation 2.2, the uncertainty in the speed is estimated as 0.1 m s⁻¹ considering uncertainties in the distance between the two spectrometer’s fields of view (Δd_Y) and in the time lag between the upper and lower column amount signals ($\Delta \tau_{lag}$) of respectively 9 m and 2 s. Δd_Y is dependent on, respectively, the uncertainties in the angle β between the two

spectrometers' fields of view, taken to be $2 \pm 0.2^\circ$ (our goniometric stage
 has a precision of 0.1° but the resulting uncertainty is considered greater
 considering imperfections in the structure supporting both spectrometers);
 the elevation angle α of the lowermost field of view which is $12 \pm 0.5^\circ$; and
 the horizontal distance D between observation site and plume which is 1960
 ± 50 m. $\Delta\tau_{lag}$ results from the common width of the cross-correlation func-
 tion maximum, which provides an estimate of the time-lag. It is important
 to note that the obtained velocity represents an average value of the plume
 speed between the two spectrometer FOVs. In reality, a deceleration of the
 plume rise is expected due to a loss of buoyancy with ascent. Moreover, the
 speed is also averaged over the length of the correlation window, used to
 estimate the time-lag, as mentioned above.

Plume velocities estimated with the DW-FOV DOAS are similar to speeds
 evaluated using video techniques. To estimate speed from the video, we
 tracked clearly defined fronts of ascending puffs (on a time scale of 30 s) and
 used for a distance scale mapped asperities on the crater rim (clearly visible
 in the video). Decreasing velocities (averaged at 30 s) were seen, in the range
 $2.8\text{--}2.1 \pm 0.4 \text{ m s}^{-1}$ for altitudes ranging from 165 to 230 m above the crater,
 which correspond approximately to the heights of the spectrometers' fields
 of view at ~ 78 and ~ 150 m (note that speeds were estimated with video
 at slightly higher altitudes than spectrometer FOVs, where puff fronts were
 better defined). The uncertainty in this speed arises from the difficulty in
 locating precisely the gas puff front (at ± 10 m), the error on the distance
 scale seen in the video field of view (estimated at 260 ± 5 m) being negligible

by comparison. It is also in agreement with theoretical estimations of the rise rate of a buoyant gas puff, which are in the range 0.6–3.2 m s⁻¹ at Erebus as shown in Appendix C.

3.3. SO₂ flux time-series

Given that the gas column amount CA_{WFOV} measured with a wide field of view spectrometer approximately represents the average column amount along the different directions in the wide angle of observation (see Section 2.2 and Appendix A), the gas flux (in kg s⁻¹) estimated with this new technique is obtained from:

$$\phi = \left(CA_{WFOV} \frac{10^4 M}{N_{Av}} \times \frac{D}{\cos \alpha} \theta_{WFOV} \right) . v, \quad (3.1)$$

considering a column amount in molec cm⁻², M the gas molar mass in kg mol⁻¹ and N_{Av} Avogadro’s number. At Erebus, the SO₂ flux measured during ~1.7 h on the 26 December 2006 varies between 0.17 and 0.89 kg s⁻¹ (Fig. 5a). The uncertainty in the flux is estimated at 0.2 kg s⁻¹ (~33% on the mean flux). This low value represents a considerable improvement in the accuracy of flux measurements. It depends on the different uncertainties, listed by order of magnitude, linked to the elevation angle of the lowermost FOV, the column amount (assumed equal to 10%), the plume speed, and the wide angle of FOV aperture (assuming an uncertainty on θ_{WFOV} of 1° resulting from the adjustment of the lenses mounted on the telescopes) leading each of them to an uncertainty in the range 0.03–0.06 kg s⁻¹ on the flux. Note that this obtained flux may include some gas emitted from a secondary vent

354 within the crater known as Werner vent, though no lava was present within
355 it during the experiment.

356 Estimations of the gas flux with the DW-FOV DOAS are similar to pre-
357 vious measurements:

- 358 • measurements of $0.86 \pm 0.20 \text{ kg s}^{-1}$ carried out in December 2003 by
359 Oppenheimer et al. (2005) by the traverse method beneath a horizon-
360 tally advected plume travelling at 5.1 m s^{-1} (the plume speed was
361 derived from two DOAS spectrometers aligned along the plume axis).
- 362 • the mean flux between 1992 and 2005 of $0.7 \pm 0.3 \text{ kg s}^{-1}$, estimated
363 by scanning vertical plumes each field season over two to five days in
364 December, with plume speeds obtained from video methods by Kyle
365 et al. (1994).

366 The SO_2 flux from Erebus is low compared to many volcanoes but is
367 similar to Erta 'Ale in Ethiopia, which also hosts a persistent lava lake (Op-
368 penheimer et al., 2004). An animation showing the results in the form of
369 an "SO₂ fluxmeter" superimposed on video of the plume, is available as an
370 electronic supplement to this article.

371 3.3.1. Time-series analysis of flux data for Erebus

372 In view of the likely non-stationarity of SO_2 output from Erebus, we
373 use wavelet analysis to explore any frequencies present in the signal, as well
374 as their variability with time. Analysis of the flux time-series is achieved
375 here using a continuous transform with a complex Morlet wavelet (Fig. 6).
376 This wavelet analysis is particularly suitable to study our non-stationary
377 time-series, where smooth variations in the frequency content are expected.

Moreover, the Fourier transform of a complex Morlet wavelet presents an analytical expression, simplifying calculations of the wavelet transform. Full details concerning the method of analysis are given in Appendix D. Concerning our time-series, high-frequencies are associated with variations of smaller amplitude of the signal than lower frequencies, and are consequently less energetic and visible in the wavelet analysis. We broadly distinguish three populations of distinctive periods, associated to approximately the same power at both spectrometers, which can be listed by decreasing energy as follows:

- Pattern 1: periods in the range 700–1300 s (~ 11 –22 min) for upper spectrometer; and in the range 800–1400 (possibly more) s (~ 13 –24 min) for lower spectrometer, which are energetic during the whole dataset.
- Pattern 2: periods in the range 300–600 s (~ 5 –10 min) for upper spectrometer, energetic until ~ 3200 s; periods in the range 400–600 s (~ 6.5 –10 min) for lower spectrometer, less energetic than at the upper instrument, present until ~ 2000 s.
- Pattern 3: periods in the range 100–200 s (~ 1.5 –2.5 min) for both spectrometers, appearing irregularly during the experiment.

Calculating the wavelet transform of both flux signals, to which a white noise of a chosen amplitude (equal to 0.1 kg s^{-1} here) has been added, allows us to test the significance of the results. The resulting wavelet analysis is slightly different but still shows peaks in power associated with the groups of periods mentioned above, including the less energetic Pattern 3 which is consequently well above the noise level and consistent. In addition, wavelet analysis was also performed on portions of the data set without gaps (i.e.

before 2000 s), verifying that these gaps, where linear interpolation was performed, do not influence the results.

4. Discussion

4.1. Methodology

The basis of the DW-FOV DOAS system to record high-temporal resolution flux measurements relies on the estimation of the plume velocity by following inhomogeneities between the two spectrometers' fields of view crossing the plume. It is consequently important to orientate fields of view closely to the perpendicular direction to plume transport in order not to gather dissimilar plume parts in a FOV. The distance between both FOVs has also to be carefully chosen in order to allow a relevant correlation analysis. It must not be too large such that structures recorded by the lower instrument are substantially modified or lost by the time they reach the upper spectrometer. The half-life of a turbulent inhomogeneity can be estimated considering the auto-correlation function of the column amount time-series where it corresponds to the width of its first peak (~ 70 s at Erebus). A large distance can also average out variations in plume speed, especially for vertical plumes which typically decelerate. Fields of view that are too close can also impede identification of elongated puffs, which cannot be adequately differentiated during their rise from the lower to the upper field of view to carry out a meaningful correlation. Depending on the plume velocity, the minimum distance of separation is also dictated by the data sampling frequency, as well as by the uncertainty of the method of correlation analysis. Furthermore, the travel time of one inhomogeneity to reach the second field of view must be

less than any periodicity of the volcanic degassing to avoid irrelevant results of the correlation analysis. As a consequence, the optimum distance between the two fields of view inside the plume will vary from one volcano to another, depending also on its activity.

Reducing the main sources of uncertainty in the gas flux estimations will improve the method. In particular, a more accurate estimation of the elevation angle of the spectrometer FOVs could be achieved quite straightforwardly. Concerning the instrument, lenses mounted on the two telescopes gave a fixed horizontal field of view width adjusted for the typical width of the Erebus plume. We have since constructed a telescopic system with adjustable fields of view to adapt to different situations. This could be particularly useful for a horizontal plume, which can display more variable dimensions with time depending on the local wind field. Vigilance is indeed required to make sure that the whole plume is captured in the wide angle of observation.

4.2. Interpretation of degassing patterns

Wavelet analysis of the flux time-series identifies three patterns in Erebus degassing (see Fig. 6 and Section 3.3.1). The most noticeable one, in terms of energy, includes periods in the range 11–24 min which are manifest during the whole data set and for both spectrometers. The second pattern is associated with 5–10 min cycles, but is only apparent during the first half of the experiment. It is relevant to note that this behaviour is more pronounced, and that the signal is stronger, in data from the upper spectrometer (see Fig. 6). This suggests that the signal results from the large scale organization of turbulence inside the plume developing with height above the crater. This is

451 commonly observed at chimneys expelling a constant gas flux where structure
 452 develops with altitude. Thus, this part of the signal yields no information
 453 about the magma source but rather the atmospheric processes modifying the
 454 large gas puffs associated with the first pattern of degassing. Further investi-
 455 gation would be required to quantify this influence and its dependence on the
 456 distance between the magmatic source and the plume sections crossed by the
 457 spectrometers' fields of view. The third pattern in degassing consists of short
 458 period fluctuations of the flux in the range 1.5–3 min, which appear several
 459 times during the experiment. They reveal the exhalations of smaller gas puffs
 460 covering just one part of the crater, as illustrated in the video (see electronic
 461 supplement). In the next section, we explore the magmatic processes that
 462 can explain the SO_2 flux variability focusing on Pattern 1, associated with
 463 cycles with 11–24 min period. Note that no explosions occurred during our
 464 observations according to seismic and acoustic observations.

465 *4.2.1. Periodic gas-rich magma supply to the lava lake*

466 Periodic SO_2 degassing could be linked to pulsatory discharge of gas-rich
 467 magma into the lava lake. Such magma flow could result from different pro-
 468 cesses. Magma convection in the conduit can promote the persistence of
 469 long-lived lava lakes with sustained degassing (Francis et al., 1993; Kaza-
 470 haya and Shinohara, 1994; Stevenson and Blake, 1998). The models assume
 471 bi-directional flow of a less dense, lower viscosity ascending magma, and a
 472 degassed, denser and more viscous descending magma. It has been shown
 473 that Erebus lava lake has a sufficiently large feeder conduit radius to maintain
 474 this process for assumed viscosity and density contrasts between rising and
 475 sinking magma (Calkins et al., 2008). Oppenheimer et al. (2009b) argued

476 that the viscosity stratification induced by such bi-directional magma flow
477 can lead to boudinage of the rising gas-rich magma and explain a pulsatory
478 supply of magma into the lake (Fig. 7a).

479

480 Variations in magma viscosity can also lead to periodic magma flow.
481 Wylie et al. (1999) have modelled magma rise dynamics assuming a constant
482 flux at the base of an elastic conduit. They showed how the dependence of
483 viscosity on volatile content can lead to an oscillating magma flow at shal-
484 low depth, given a relevant range of model input parameters (Fig. 7b). This
485 model was applied to the andesitic Soufriere Hills Volcano (Montserrat), indi-
486 cating an unstable magma flow with oscillation periods of a few hours, but it
487 should be valid more generally during closed system degassing. However, no
488 analytical expression is given for the oscillation frequency. Thus we cannot
489 identify if it reproduces the 11–24 min periodic degassing observed at Ere-
490 bus, but it does provide a plausible conceptual mechanism. Periodic magma
491 flow could also result from pressurization feedbacks between magma ascent
492 rate, crystallization, and open *vs.* closed-system degassing, which have been
493 proposed as an explanation for the periodic behaviour of andesitic and silicic
494 domes (Melnik and Sparks, 1999; Barmin et al., 2002).

495 A further explanation for periodic magma ascent is stick-slip movement
496 along the conduit walls (Denlinger and Hoblitt, 1999). This mechanism
497 can be ruled out for Erebus given the absence of corresponding seismicity
498 – the few long period earthquakes that are recorded there are associated
499 with Strombolian explosions (Aster et al., 2003, 2008).

500 4.2.2. *Periodic gas supply to the lava lake*

501 Gas segregation at the roof of a magma reservoir (Jaupart and Vergnolle,
502 1989) or in asperities such as horizontal intrusions leading from a magma
503 conduit (Menand and Phillips, 2006), has been suggested to explain inter-
504 mittent Strombolian explosions. This mechanism considers the progressive
505 accumulation of a gas foam that grows and becomes unstable above a critical
506 thickness. The foam then collapses as bubbles coalesce, resulting in expul-
507 sion of overpressured gas slugs that rise to the surface generating explosions.
508 Since there were no explosions at Erebus during the period of our experi-
509 ment, we consider a variation of this process that might result in periodic
510 passive degassing. Rather than an asperity with sharp boundaries, we con-
511 sider a continuous, smooth cavity in the conduit walls, as illustrated in Fig.
512 7c. The gas expelled to the atmosphere is then a mixture of two sources:
513 one, a continuous degassing from a magma rising directly from depth to sur-
514 face; the other associated with the accumulation of gas in a smooth conduit
515 cavity, which depends on the size of this segregator as well as the rising gas
516 and magma fluxes. This smooth geometry does not allow the collapse of a
517 gas foam but rather the regular retention and extraction of the accumulating
518 foam. This would permit a continuous passive release of gas from the lava
519 lake with a periodic pattern depending on the rate of gas accumulation at
520 some depth in the magmatic system.

521 4.2.3. *Complementary geochemical and geophysical observations*

522 These two groups of physical processes allow us to interpret not only the
523 observed periodic flux of SO_2 but also diverse geochemical and geophysical
524 measurements made during other field seasons at Erebus. Unfortunately,

525 when our DW-FOV DOAS spectra were recorded in December 2006, it was
 526 already late in the field season and other instruments (thermal camera and
 527 FTIR spectrometer) were not running; so we cannot explore the correlation
 528 between the time varying behaviour of gas flux with other parameters. Nev-
 529 ertheless, it is of particular interest to note that a similar periodicity of about
 530 10 min has been identified in December 2004 from analysis of both thermal
 531 imagery of the lava lake and gas composition measured by Fourier transform
 532 infrared spectroscopy (Oppenheimer et al., 2009b). These observations re-
 533 vealed cycles in lava lake convection (surface speed and direction) and heat
 534 output with periods of 4–15 min, that were phase-locked with cyclic changes
 535 in gas composition (SO_2/CO_2 and HCl/CO ratios). Column amounts of gases
 536 measured between the crater rim and the lake surface (a distance of about
 537 300 m) also revealed the same cyclicity, suggesting that gas fluxes were very
 538 likely periodic too. Both types of model discussed above can account for
 539 these additional observations but only gas segregation offers an explanation
 540 for the seismicity at Erebus and complementary geochemical measurements.
 541 The stability of oscillatory, very long period signals preceding Strombolian
 542 eruptions, over a span of five years, suggests a stable near-summit reservoir
 543 with multiple sites for gas slug coalescence as VLP sources (Aster et al., 2003,
 544 2008). Shallow magma sequestration is also proposed to interpret measure-
 545 ments of water and carbon dioxide fluxes from Erebus, which reveal that not
 546 all the magma that supplies the CO_2 emitted from the lake can reach the
 547 surface, since otherwise the H_2O flux should be much higher than observed
 548 (Oppenheimer and Kyle, 2008). Note that the presence of a CO_2 rich pre-
 549 existing fluid phase, not trapped in melt inclusions, could also explain this

550 observation.

551 *4.3. Further remarks*

552 This study shows the value of accurate high resolution flux data to explore
553 variability in magma degassing. Our experiment was only of short-duration
554 and we only had simultaneous video images as additional data. This pre-
555 cludes discrimination between the alternative models for the periodic de-
556 gassing behaviour of Erebus that we identified. However, it paves the way
557 for further investigation, which will greatly benefit from complementary vol-
558 canological observations including thermal imagery, and FTIR spectroscopy
559 to constrain the depths of gas sources in the magmatic network, the mecha-
560 nisms of gas segregation, and the different modes of gas transport. A better
561 knowledge of the magma plumbing system with the dimension of potential
562 gas storage regions could be explored further through seismic studies. Even-
563 tually, developing physical models from conceptual mechanisms will help to
564 determine the range of input parameters (including in particular rising gas
565 and magma fluxes, magma rheology, the dimension of gas bubbles, and the
566 geometry and size of gas segregators) that would lead to periodic degassing,
567 and how the expected periodicity at Erebus could be modelled analytically.

568 **5. Conclusions**

569 We have described the construction of a dual wide field of view UV spec-
570 troscopic system designed for the high temporal resolution measurement of
571 volcanic gas fluxes (principally of the species SO_2). The novelty of the in-
572 strumental set up lies in the use of a combination of spherical and cylindrical

573 lenses, which present an elongated field of view that is oriented perpendic-
574 ularly to the plume transport direction so as to observe all SO₂ molecules
575 present simultaneously (without the need for imaging, motion or scanning).
576 Additionally, the two fields of view are separated by a small angle that per-
577 mits tracking of plume inhomogeneities in the time-stamped datasets ob-
578 tained from each spectrometer. The data analysis includes DOAS retrieval
579 of gas column amounts and correlation analysis of the time-varying signals
580 recorded at the two spectrometers, whose angular separation indicates the
581 separation distance between the two instrument fields of view projected to
582 the plume. The deployment of the system is relatively simple and it can
583 be used, in principle, on any plume rising vertically or drifting horizontally,
584 where the basic plume and viewing geometry can be measured with some
585 certainty. Processing of the data could also be achieved in real-time, and it
586 would only require limited further development to yield a real-time flux me-
587 ter, capable of measurements at a frequency of 1 Hz or better, with accuracy
588 of 33% or better.

589 This method allows the study of short-term variations in volcanic de-
590 gassing. We have demonstrated the vigilance required to discriminate be-
591 tween fluctuations linked to atmospheric processes from those resulting from
592 magmatic activity. At Erebus, a particularly noticeable periodicity in the
593 range 11–24 min is apparent in the SO₂ degassing rate. Two groups of phys-
594 ical processes can explain this oscillatory behaviour. The first involves a
595 periodic supply of gas-rich magma to the lava lake, which may result either
596 from boudinage of the rising magma flow due to shear stresses between as-
597 cending and descending magmas in a bi-directional conduit flow, or from a

598 volatile-dependent viscosity leading to an oscillating magma flow. The sec-
 599 ond mechanism is associated with periodic supply of gas to the lake arising
 600 from gas segregation in smooth cavities in the conduit. Smaller gas puffs,
 601 leading to short-period fluctuations of the flux lasting a few minutes, are
 602 also observed intermittently. A longer experiment duration, combining flux
 603 measurements with other volcanological data streams, is needed to discrimi-
 604 nate between the suggested source mechanisms for this particular degassing
 605 behavior. This would improve understanding of gas and magma dynamics
 606 and storage in the Erebus plumbing system.

607 **A. Meaning of the column amount measured with DW-FOV DOAS** 608 **spectrometers**

609 The elemental light power $d\Phi$ received from the solid angle $d\Omega$, associated
 610 to longitude θ and latitude α , by a lens aperture of surface A_r is a function
 611 of the radiance (or intensity) L :

$$d\Phi = A_r L(\theta, \alpha) d\Omega. \quad (\text{A.1})$$

612

613 Considering a small lens aperture surface, the total light power received
 614 by a wide field of view capturing instantaneously the whole horizontal plume
 615 cross-section spectrometer is given by:

$$\Phi = A_r \int_{-\theta_{NFOV}/2}^{+\theta_{NFOV}/2} \int_{-\theta_{WFOV}/2}^{+\theta_{WFOV}/2} L(\theta, \alpha) d\Omega, \quad (\text{A.2})$$

616

617 where θ_{WFOV} and θ_{NFOV} are, respectively, the wide horizontal and narrow
 618 vertical angles of aperture of the field of view. The elemental solid angle can
 619 be written in spherical coordinates:

$$d\Omega = \cos\alpha d\theta d\alpha. \quad (\text{A.3})$$

620
 621 The vertical angle of aperture of the wide field of view spectrometers
 622 θ_{NFOV} being very small (8 mrad), the radiance can be assumed constant on
 623 the range of considered latitudes α . The total light power (Eq. A.2) is thus
 624 given by:

$$\Phi = A_r \theta_{NFOV} \int_{-\theta_{wfov}/2}^{+\theta_{wfov}/2} L(\theta) d\theta, \quad (\text{A.4})$$

625
 626 and can be rewritten:

$$\Phi = A_r \theta_{NFOV} \theta_{WFOV} \bar{L}(\theta), \quad (\text{A.5})$$

627
 628 with \bar{L} the mean radiance for $\theta \in [-\theta_{WFOV}/2; \theta_{WFOV}/2]$. An equivalent
 629 equation is valid for the light power received from the background sky

$$\Phi_{bg} = A_r \theta_{NFOV} \theta_{WFOV} \bar{L}_{bg}(\theta). \quad (\text{A.6})$$

630
 631 Combining Eq. A.5 and A.6, we have:

$$\frac{\Phi}{\Phi_{Bg}} = \frac{\bar{L}}{\bar{L}_{bg}}. \quad (\text{A.7})$$

632

633 Moreover, according to the Beer-Lambert law (simplified here by not
634 explicitly including low-frequency components), we have:

$$L(\theta) = L_{bg}(\theta)e^{-\sigma CA(\theta)}, \quad (\text{A.8})$$

635

636 where σ is the cross-section of the considered gas species and $CA(\theta)$ its
637 slant column amount in the direction defined by θ . Note that the proof is
638 exactly the same with the complete Beer-Lambert law, merely an additional
639 step is required to remove the low-frequency component. We would obtain in
640 this case the above equation, where σ would just be replaced by its associated
641 differential cross section. A limited development of the exponential is valid
642 for Eq. A.8 if we have weak optical depths (i.e. $\sigma CA(\theta) \ll 1$). This is the
643 case at Erebus considering the emission of sulfur dioxide, where this product
644 is close to 10^{-2} , with a SO_2 slant column amount of the order of 10^{17} molec
645 cm^{-2} and $\sigma_{\text{SO}_2} \sim 10^{-19} \text{ cm}^2$. It follows that:

$$L(\theta) \sim L_{bg}(\theta)(1 - \sigma CA(\theta)). \quad (\text{A.9})$$

646

647 If we take the mean of this expression with θ , assuming that the back-
648 ground has been collected for a uniform or clear sky and that L_{bg} is conse-
649 quently negligibly dependent on θ , we find:

$$\bar{L} \sim L_{bg}(1 - \sigma\overline{CA}). \quad (\text{A.10})$$

650

651 Therefore, Eq. A.7 can be rewritten:

$$\frac{\Phi}{\Phi_{Bg}} \sim (1 - \sigma\overline{CA}). \quad (\text{A.11})$$

652

653 Given again ($\sigma\overline{CA} \ll 1$), Eq. A.11 is approximated by:

$$\Phi \sim \Phi_{bg}e^{-\sigma\overline{CA}}, \quad (\text{A.12})$$

654

655 with

$$\overline{CA} = \frac{1}{\theta_{WFOV}} \int_{-\theta_{WFOV}/2}^{+\theta_{WFOV}/2} CA(\theta) d\theta. \quad (\text{A.13})$$

656

657 Consequently, the column amount measured with the wide field of view
 658 spectrometer CA_{WFOV} represents the mean column amount along the differ-
 659 ent directions θ inside the wide angle of observation θ_{WFOV} . This result has
 660 been proved assuming weak optical depths here. But it is generally valid, for
 661 any optical depth. In this case, we cannot give an analytical expression for
 662 the relationship between CA_{WFOV} and \overline{CA} . But we can estimate the error
 663 made when assuming the equality $CA_{WFOV} = \overline{CA}$, that will be used then
 664 for gas flux estimation with this technique. According to Eq. A.7 and the
 665 simplified Beer Bouguer Lambert law Eq. A.8, we have:

$$e^{-\sigma CA_{WFOV}} = \overline{e^{-\sigma CA(\theta)}}. \quad (\text{A.14})$$

Moreover, a first order Taylor expansion with integral remainder gives:

$$e^{-\sigma CA_{WFOV}} = 1 - \sigma CA_{WFOV} + \int_0^{\sigma CA_{WFOV}} (\sigma CA_{WFOV} - t)e^{-t} dt \quad (\text{A.15})$$

and

$$\overline{e^{-\sigma CA(\theta)}} = 1 - \sigma \overline{CA(\theta)} + \overline{\int_0^{\sigma CA(\theta)} (\sigma CA(\theta) - t)e^{-t} dt}. \quad (\text{A.16})$$

As a consequence, writing Eq. A.14 from Eq. A.15 and A.16 gives the error made by approximating CA_{WFOV} by \overline{CA} :

$$CA_{WFOV} - \overline{CA(\theta)} = \frac{1}{\sigma} \left(\int_0^{\sigma CA_{WFOV}} (\sigma CA_{WFOV} - t)e^{-t} dt - \overline{\int_0^{\sigma CA(\theta)} (\sigma CA(\theta) - t)e^{-t} dt} \right), \quad (\text{A.17})$$

which gives after majoration

$$\left| \frac{CA_{WFOV} - \overline{CA(\theta)}}{\overline{CA(\theta)}} \right| \leq \sigma \max_{\theta}(CA). \quad (\text{A.18})$$

Fig. 8 illustrates the evolution of this relative error according to the strength of gas emission from the studied volcano.

B. Cases of failure of the correlation analysis linked to plume characteristics

Correlation analysis is successful when clearly defined structures are present in the selected window. But failures show up in the following cases:

- 677 • when a structure in the degassing is recorded at the first spectrometer
678 but has faded or completely dissipated by the time it reaches the second
679 spectrometer.
- 680 • when there is no structure in the plume. In this case, the maximum
681 of the *CCF* function which is obtained is not meaningful due to the
682 presence of a few peaks with similar amplitudes. Checking the video
683 footage recorded simultaneously with the DOAS measurements, we ob-
684 served that these limits in the correlation analysis do occur when the
685 plume appears less distinct with elongated and very few structured
686 puffs, as opposed to smaller puffs with a clearly defined rise front due
687 to a large contrast of density with the surrounding air.

688 **C. Theoretical estimation of a rise speed of a buoyant puff**

689 According to seismic observations, there were no explosions during our
690 period of spectroscopic measurements and degassing consisted of the passive
691 release of magmatic gases from the lava lake. The rise of these hot gas
692 puffs, or thermals, is consequently mainly driven by buoyancy and not by an
693 initial source momentum. Their ascent, during which they rapidly entrain
694 colder atmospheric air through a large organized vortex ring and expand,
695 can be described by fluid dynamics. If a fully turbulent regime is assumed,
696 an analytical solution of the three coupled equations of mass, momentum
697 and energy conservation is possible. It is self-similar with distance from
698 the source z and for a non density stratified atmosphere can be written as
699 (Morton et al., 1955; Turner, 1979; Sparks et al., 1997; Branan et al., 2008):

$$r = \epsilon z \quad (\text{C.1})$$

$$v = \left(\frac{B_0 r_0^3}{3\epsilon^3} \right)^{1/2} \frac{1}{z} \quad (\text{C.2})$$

$$B = \frac{B_0 r_0^3}{\epsilon^3} \frac{1}{z^3} \quad (\text{C.3})$$

700

701 with the expression of the buoyancy

$$B = g \left(\frac{\rho_a - \rho_p}{\rho_{a0}} \right), \quad (\text{C.4})$$

702

703 where r is the radius of the puff which is assumed spherical, v its vertical
 704 velocity, ϵ the entrainment constant (with an empirically determined value
 705 of 0.25 for fully turbulent laboratory thermals (Scorer, 1957; Turner, 1979)),
 706 g the acceleration due to gravity, ρ_p and ρ_a the bulk density of, respectively,
 707 the puff and the surrounding atmospheric air. The subscript 0 refers to the
 708 variable value at the source of the puff release, which is the lava lake at
 709 Erebus.

710 Note that an idealized point source is an unrealistic initial condition. This
 711 flow description is consequently not valid very close to the source. We show
 712 that it can be applied at the altitude of the DOAS measurements, just
 713 above the crater rim (~ 220 m above the lake). Indeed, this model predicts
 714 spherical puffs with a radius of 55 m, which is consistent with estimates made
 715 from available photographs and video where it varies between 45 and 68 m.
 716 According to Eq. C.2, the puff vertical speed mainly depends on the source

radius r_0 via an exponent of 3, and at second order on the reduced gravity B_0 .

An upper value for the source size is the dimension of the lava lake whose the radius is ~ 17.5 m. A better constrained range of estimates can also be deduced from the dilution coefficient d , defined as the ratio of the initial puff volume to the volume at the measurement height, which can be written:

$$d = \left(\frac{r_0}{r} \right)^3. \quad (\text{C.5})$$

From Fourier Transform Infrared (FTIR) spectroscopy carried out from the crater rim along the 300 m path to the lava lake, a mean mixing ratio of ~ 0.001 is evaluated and gives a rough indication of the dilution coefficient which can be assumed to range in 0.01–0.001. According to photographs, for a puff radius at the measurement altitude of 44–68 m, Eq. C.5 gives a source radius in the range 4.5–14.5 m.

The puff consists of a gas mixture (10 kg s^{-1} of water; 15 kg s^{-1} of CO_2 , total gas flux of 27 kg s^{-1}) (Oppenheimer and Kyle, 2008), whose density follows the perfect gas law. Its value at the source is $\sim 0.2 \text{ kg m}^{-3}$ for an initial puff temperature of 1273 K, an atmospheric air temperature of 250 K and pressure of $\sim 0.63 \cdot 10^5 \text{ Pa}$ for Erebus summit altitude (3798 m above sea level). From Eq. C.2, assuming an atmospheric bulk density of 0.88 kg m^{-3} , the puff vertical velocity is in the range $0.6\text{--}3.2 \text{ m s}^{-1}$.

Note that the assumption of a turbulent regime can be checked afterwards. The Reynolds number associated with the puff rise dynamics has the expression:

$$Re_P = \frac{vz\rho_P}{\mu_P}, \quad (\text{C.6})$$

740

741 where μ_P represents the gas puff dynamic viscosity (of $\sim 5 \times 10^{-6}$ Pa s
 742 according to Sutherland's formula describing viscosity variations with tem-
 743 perature, though this calculation is made outside the calibration range for a
 744 temperature of 555 K and thus represents an approximation). For a mean
 745 vertical speed of 2 m s^{-1} , Re_P is $\sim 10^7$ at the measurement height, i.e. much
 746 greater than 10^4 and demonstrating a fully turbulent flow.

747 This description of the plume rise does not consider the potential convec-
 748 tive flux of air that is heated by the surface of the lava lake. It can reduce the
 749 contrast of temperature between the puff and the surrounding air, slowing
 750 the puff rise. On the other hand, it can also entrain the puff and accelerate
 751 its ascent. This effect has counterbalancing consequences and is neglected.

752 D. Wavelet analysis

753 A time-series analysis is performed using a complex Morlet wavelet with
 754 the expression

$$\Psi(t) = \frac{1}{\pi^{1/4}} (e^{+i\omega_0 t} - e^{-i\omega_0^2/2}) e^{-t^2/2}. \quad (\text{D.1})$$

755

756 ω_0 is taken equal to 2π and is consequently superior to 5 in order to
 757 satisfy the wavelet admissibility condition (Farge, 1992). The second term
 758 of Eq. D.1 is also thus negligible and the Fourier transform of this wavelet is
 759 simply a Gaussian function, which facilitates the calculation of the wavelet

transform (Torrence and Compo, 1998). We chose to express the wavelet analysis as a function of a set of scales a linearly distributed between T_{min} and T_{max} , which represent the shortest and longest time periods that we can study. They are, respectively, taken as equal to twice the time spacing of the dataset (1 s here) and less than half the duration of the entire data set (~ 4000 s), in order to satisfy the Nyquist-Shannon sampling theorem. Note that the scales associated with a Morlet wavelet are almost equal to Fourier periods for $\omega_0 \sim 6$ (Torrence and Compo, 1998). This analysis is carried out on flux time-series that are linearly interpolated to fill the few data gaps in plume speed estimations resulting from the lack of plume structure, assuming continuous variations of the velocity. The domain where the wavelet analysis does not suffer from edge effects is delimited by a cone of influence. It is associated with a characteristic time equal to $\sqrt{2}a$, which corresponds to the time where the wavelet power associated to a discontinuity at the edge drops by a factor e^{-2} , which ensures that the edge effect is negligible (Torrence and Compo, 1998).

Acknowledgments

We gratefully acknowledge support from NSF Office of Polar Programs grants (OPP-0229305; ANT-0538414) and the United States Antarctic Program. CO also thanks the Leverhulme Trust for a Study Abroad Fellowship and the EU Framework 6 programme, which supported the project NOVAC. MB thanks the European Commission for an Intra-European Marie-Curie Fellowship (Project VolcanGas 14018), and Olivier De Viron for fruitful discussions concerning signal analysis. CO and PK warmly acknowledge their

784 companions in Science Event G-081 and the helicopter pilots, and staff based
785 at McMurdo Station. They particularly thank Dr. Tom Wagner (then NSF
786 Program Manager for Antarctic Geology and Geophysics) for support.

787 **References**

- 788 Aster, R., Mah, S., Kyle, P., McIntosh, W., Dunbar, N., Johnson, J., Ruiz,
789 M., McNamara, S., 2003. Very long period oscillations of Mount Erebus
790 Volcano. *J. Geophys. Res.* 108 (B11, 2552).
- 791 Aster, R., Zandomenighi, D., Mah, S., McNamara, S., Henderson, D., Knox,
792 H., Jones, K., 2008. Moment tensor inversion of very long period seis-
793 mic signals from Strombolian eruptions of Erebus Volcano. *J. Volcanol.*
794 *Geotherm. Res.* 177, 635–647.
- 795 Barmin, A., Melnik, O., Sparks, R., 2002. Periodic behavior in lava dome
796 eruptions. *Earth Planet. Sci. Lett.* 199, 173–184.
- 797 Bluth, G., Shannon, J., Watson, I., Prata, A., Realmuto, V., 2007. De-
798 velopment of an ultra-violet digital camera for volcanic SO₂ imaging. *J.*
799 *Volcanol. Geotherm. Res.* 161, 47–56.
- 800 Bobrowski, N., Honninger, G., Lohberger, F., Platt, U., 2006. IDOAS: a
801 new monitoring technique to study the 2D distribution of volcanic gas
802 emissions. *J. Volcanol. Geotherm. Res.* 150, 47–56.
- 803 Bogumil, K., Orphal, J., Homann, T., Voigt, S., Spietz, P., Fleischmann, O.,
804 Vogel, A., Hartmann, M., Kromminga, H., Bovensmann, H., Frerick, J.,
805 Burrows, J., 2003. Measurements of molecular absorption spectra with the

806 SCIAMACHY pre-flight model: instrument characterization and reference
807 data for atmospheric remote-sensing in the 230-2380 nm region. *Journal*
808 *of Photochemistry and Photobiology A: Chemistry* 157, 167–184.

809 Branan, Y., Harris, A., Watson, M., Phillips, J., Horton, K., Williams-Jones,
810 G., Garbeil, H., 2008. Investigation of at-vent dynamics and dilution using
811 thermal infrared radiometers at Masaya volcano, Nicaragua. *J. Volcanol.*
812 *Geotherm. Res.* 169, 34–47.

813 Burrows, J., Richter, A., Dehn, A., Deters, B., Himmelmann, S., Voight, S.,
814 Orphal, J., 1999. Atmospheric remote-sensing reference data from GOME.
815 2- Temperature-dependent absorption cross sections of O₃ in the 231-794
816 nm range. *J. Quant. Spectrosc. Radiat. Transfer* 61 (4), 509–517.

817 Burton, M., Allard, P., Mur, F., La Spina, A., 2007. Magmatic gas composi-
818 tion reveals the source depth of slug-driven Strombolian explosive activity.
819 *Science* 317, 227–230.

820 Calkins, J., Oppenheimer, C., Kyle, P., 2008. Ground-based thermal imaging
821 of lava lakes at Erebus volcano, Antarctica. *J. Volcanol. Geotherm. Res.*

822 Denlinger, R., Hoblitt, R., 1999. Cyclic eruptive behavior of silicic volcanoes.
823 *Geology* 5, 459–462.

824 Edmonds, M., Herd, R., Galle, B., Oppenheimer, C., 2003. Automated,
825 high time-resolution measurements of SO₂ flux at Soufriere Hills Volcano,
826 Montserrat. *Bull. Volcanol.* 65, 578–586.

827 Farge, M., 1992. Wavelet transforms and their applications to turbulence.
828 *Annu. Rev. Fluid Mech.* 24, 395–457.

829 Fiorani, L., Colao, F., Palucci, A., 2009. Measurement of Mount Etna plume
830 by CO₂-laser-based lidar. *Optics Letters* 34 (6), 800–802.

831 Fischer, T., Morrissey, M., V., M. L. C., M., D. G., C., R. T., Stix, J.,
832 Williams, S., 1994. Correlations between SO₂ flux and long-period seis-
833 micity at Galeras Volcano. *Nature* 368, 135–137.

834 Fischer, T., Roggensack, K., Kyle, P., 2002. Open and almost shut case for
835 explosive eruptions: vent processes determined by SO₂ emission rates at
836 Karymsky volcano, Kamchatka. *Geology* 30 (12), 1059–1062.

837 Francis, P., Oppenheimer, C., Stevenson, D., 1993. Endogenous growth of
838 persistently active volcanoes. *Nature* 366, 554–557.

839 Galle, B., Oppenheimer, C., Geyer, A., McGonigle, A., Edmonds, M., Hor-
840 rocks, L., 2003. A miniaturised ultraviolet spectrometer for remote sensing
841 of SO₂ fluxes: a new tool for volcano surveillance. *J. Volcanol. Geoth. Res.*
842 119, 241–254.

843 Harris, A., Carniel, R., Jones, J., 2005. Identification of variable convective
844 regimes of Erta 'Ale Lava Lake. *J. Volcanol. Geotherm. Res.* 142, 207–223.

845 Hausmann, M., Brandenburger, U., Brauers, T., Dorn, H., 1999. Sim-
846 ple monte carlo methods to estimate the spectra evaluation error in
847 differential-optical-absorption spectroscopy. *Applied Optics* 38 (3), 462–
848 475.

849 Jaupart, C., Vergnolle, S., 1989. The generation and collapse of a foam layer
850 at the roof of a basaltic magma chamber. *J. Fluid Mech.* 203, 347–380.

851 Johansson, M., Galle, B., Zhang, Y., Rivera, C., Chen, D., Wyser, K., 2009.
852 The dual-beam mini-DOAS technique, measurements of volcanic gas emis-
853 sion, plume height and plume speed with a single instrument. Bull. Vol-
854 canol. in press.

855 Kazahaya, K., Shinohara, H., 1994. Excessive degassing of Izu-Oshima vol-
856 cano: magma convection in a conduit. Bull. Volcanol 56, 207–216.

857 Kern, C., Deutschmann, T., Vogel, L., Wohrbach, M., Wagner, T., Platt, U.,
858 2009. Radiative transfer corrections for accurate spectroscopic measure-
859 ments of volcanic gas emissions. Bull. Volcanol., 1241–1253.

860 Kyle, P., Sybeldon, L., McIntosh, W., Meeker, K., Symonds, R., 1994. Sul-
861 fur dioxide emission rates from Mount Erebus, Antarctica. In: Kyle, P.R.
862 (Ed.), Volcanological and Environmental Studies of Mount Erebus, Antarc-
863 tica. Vol. 213. American Geophysical Union, Washington, D.C., pp. 69–
864 82.

865 McGonigle, A., Hilton, D., Fischer, T., Oppenheimer, C., 2005a. Plume ve-
866 locity determination for volcanic SO₂ flux measurements. Geophys. Res.
867 Lett. 32.

868 McGonigle, A., Inguaggiato, S., Aiuppa, A., Hayes, A., Oppenheimer, C.,
869 2005b. Accurate measurement of volcanic SO₂ flux: determination of plum
870 transport speed and integrated SO₂ concentration with a single device.
871 Geochem. Geophys. Geosyst. 6 (Q02003).

872 McGonigle, A., Oppenheimer, C., 2003. Optical sensing of volcanic gas and
873 aerosol emissions. In: Oppenheimer, C. and Pyle, D.M. and Barclay J.

874 (Ed.), Volcanic Degassing. Vol. 213. Geological Society, London, Special
875 Publications, pp. 149–168.

876 Melnik, O., Sparks, R., 1999. Non linear dynamics of lava dome extrusion.
877 Nature 402, 37–41.

878 Menand, T., Phillips, J., 2006. Gas segregation in dykes and sills. J. Volcanol.
879 Geotherm. Res.

880 Millan, M., 1980. Remote sensing of air pollutants, a study of some atmo-
881 spheric scattering effects. *Atm. Environ.* 14 (11), 1241–1253.

882 Moffat, A., Millan, M., 1971. The applications of optical correlation tech-
883 niques to the remote sensing of SO₂ plumes using sky light. *Atm. Environ.*
884 5, 677–690.

885 Mori, T., Burton, M., 2006. The SO₂ camera: a simple, fast and cheap
886 method for ground-based imaging of SO₂ in volcanic plumes. *Geophys.*
887 *Res. Lett.* 33 (L24804).

888 Mori, T., Mori, T., Kazahaya, K., Ohwada, M., Hirabayashi, J., Yoshikawa,
889 S., 2006. Effect of UV scattering on SO₂ emission rate measurements. *Geo-*
890 *phys. Res. Let.* 33 (L17315).

891 Morton, B., Taylor, G., Turner, J., 1955. Turbulent gravitational convection
892 from maintained and instantaneous sources. *Proc. R. Soc. Lond.* 234, 1–23.

893 Oppenheimer, C., 2003. Volcanic degassing. In: Holland, H., Turekian, K.
894 (Eds.), *The crust, treatise on geochemistry*. Vol. 3. Elsevier-Pergamon,
895 Oxford, Ch. 3.04, pp. 123–166.

896 Oppenheimer, C., Bani, P., Calkins, J., Burton, M., Sawyer, G., 2006. Rapid
897 FTIR sensing of volcanic gases released by Strombolian explosions at Yasur
898 volcano, Vanuatu. *Applied Physics B*. 85, 453–460.

899 Oppenheimer, C., Kyle, P., 2008. Probing the magma plumbing of Erebus
900 volcano, Antarctica, by open-path FTIR spectroscopy of gas emissions. *J.*
901 *Volcanol. Geotherm. Res.* 177, 743–754.

902 Oppenheimer, C., Kyle, P., Eisele, F., Crawford, J., Huey, G., Tanner, D.,
903 Brady, K., Mauldin, L., Blake, D., Beyersdorf, A., Buhr, M., Davis, D.,
904 2009a. Atmospheric chemistry of an Antarctic volcanic plume. *J. Geophys.*
905 *Res. Atm.*, –.

906 Oppenheimer, C., Kyle, P., Tsanev, V., McGonigle, A., Mather, T., Sweeney,
907 D., 2005. Mt. Erebus, the largest point source of NO_2 in Antarctica. *Atm.*
908 *Environ.* 39, 6000–6006.

909 Oppenheimer, C., Lomakina, A., Kyle, P., Kingsbury, N., Boichu, M., 2009b.
910 Pulsatory magma supply to Erebus lava lake, Antarctica. *Earth Planet.*
911 *Sci. Lett.* 284, 392–398.

912 Oppenheimer, C., McGonigle, A., Allard, P., Wooster, M., Tsanev, V., 2004.
913 Sulfur, heat and magma budget of Erta 'Ale lava lake, Ethiopia. *Geology*
914 32 (6), 509–512.

915 Platt, U., Marquard, L., Wagner, T., Perner, D., 1997. Corrections for zenith
916 scattered light DOAS. *Geophys. Res. Lett.* 24 (14), 1759–1762.

917 Platt, U., Stutz, J., 2008. Differential Optical Absorption Spectroscopy:
918 Principles and Applications. Springer, Berlin.

- 919 Radke, L., 1982. Chlorine, fluorine, and sulfur emissions from Mount Ere-
920 bus, Antarctica and estimated contributions to the Antarctic atmosphere.
921 Nature 299, 710–712.
- 922 Scorer, R., 1957. Experiments on convection of isolated masses of buoyant
923 fluid. J. Fluid Mech. 2, 583–594.
- 924 Sparks, R., Bursik, M., Carey, S., Gilbert, J., Glaze, L., Sigurdsson, H.,
925 Woods, A., 1997. Volcanic Plumes. John Wiley and Sons, New-York.
- 926 Stevenson, D., Blake, S., 1998. Modelling the dynamics and thermodynamics
927 of volcanic degassing. Bull. of Volcanol. 60, 307–317.
- 928 Stoiber, R. E., Jepsen, A., 1973. Sulfur dioxide contributions to the atmo-
929 sphere by volcanoes. Science 182 (4112), 577–578.
- 930 Stoiber, R. E., Malinconico, L., Williams, S., 1983. Use of the correlation
931 spectrometer at volcanoes. In: Tazieff, H. and Sabroux, J.C. (Ed.), Fore-
932 casting Volcanic Events. Elsevier Sci., New York, pp. 425–444.
- 933 Stutz, J., Platt, U., 1996. Numerical analysis and estimation of the statistical
934 error of differential optical absorption spectroscopy measurements with
935 least-squares methods. Applied Optics 35 (30), 6041–6053.
- 936 Sweeney, D., Kyle, P., Oppenheimer, C., 2008. Sulfur dioxide emissions and
937 degassing behavior of Erebus volcano, Antarctica. J. Volcanol. Geotherm.
938 Res. 177, 725–733.
- 939 Symonds, R., Gerlach, T., M.H., R., 2001. Magmatic gas scrubbing: impli-
940 cations for volcano monitoring. J. Volcanol. Geotherm. Res. 108, 303–341.

941 Torrence, C., Compo, G., 1998. A practical guide to wavelet analysis. *Bull.*
942 *Am. Meteo. Soc.* 79 (1), 61–78.

943 Turner, J., 1979. *Buoyancy effects in fluids*. Cambridge University Press.

944 Watson, I., Oppenheimer, C., Voight, B., Francis, P., Clarke, A., Stix, J.,
945 Miller, A., Pyle, D., Burton, M., Young, S., Norton, G., Loughlin, S., Dar-
946 roux, B., Staff, M., 2000. The relationship between degassing and ground
947 deformation at Soufriere Hills Volcano, Montserrat. *J. Volcanol. Geotherm.*
948 *Res.* 98, 117–126.

949 Williams-Jones, G., Horton, K., Elias, T., Garbeil, H., Mougini-Mark, P.,
950 Sutton, A., Harris, A., 2006. Accurately measuring volcanic plume velocity
951 with multiple UV spectrometers. *Bull. Volcanol.* 68, 328–332.

952 Wylie, J., Voight, B., Whitehead, J., 1999. Instability of magma flow from
953 volatile-dependent viscosity. *Science* 285, 1883–1885.

954 Young, S., Voight, B., Duffell, H., 2003. Magma extrusion dynamics revealed
955 by high-frequency gas monitoring at Soufriere Hills volcano, Montserrat.
956 In: Oppenheimer, C. and Pyle, D.M. and Barclay, J. (Ed.), *Volcanic De-*
957 *gassing*. Vol. 213. Geological Society, London, Special Publications, pp.
958 219–230.

959 Zreda-Gostynska, G., Kyle, P., Finnegan, D., Prestbo, K., 1993. Chlorine,
960 fluorine, and sulfur emissions from Mount Erebus, Antarctica and esti-
961 mated contributions to the Antarctic atmosphere. *Geophys. Res. Lett.* 20,
962 1959–1962.

Table 1: Symbols used.

α	Elevation angle of the lowermost field of view, in deg.
θ_{NFOV}	Narrow angle of aperture of the spectrometers fields of view, in deg.
β	Angle of separation between the two fields of view, in deg.
d_X	Long horizontal axis of the field of view at the plume distance, in m.
d_Y	Vertical distance between the two fields of view at the plume distance, in m.
D	Horizontal distance between observation site and plume, in m.
CCF	Cross correlation function
Δt	Time step of the gas column amount series, in s.
$\Delta \tau$	Time resolution of the correlation analysis, in s.
ΔT	Duration of correlation sliding windows, in s.
t	Time, in s.
τ	Time shift of the correlation window for the upper spectrometer signal, in s.
θ_{WFOV}	Wide angle of aperture of the spectrometer fields of view, in deg.

963 Zreda-Gostynska, G., Kyle, P., Finnegan, D., Prestbo, K., 1997. Volcanic gas
964 emissions from Mount Erebus and their impact on the Antarctic environ-
965 ment. J. Geophys. Res. 102 (B7), 15039–15056.

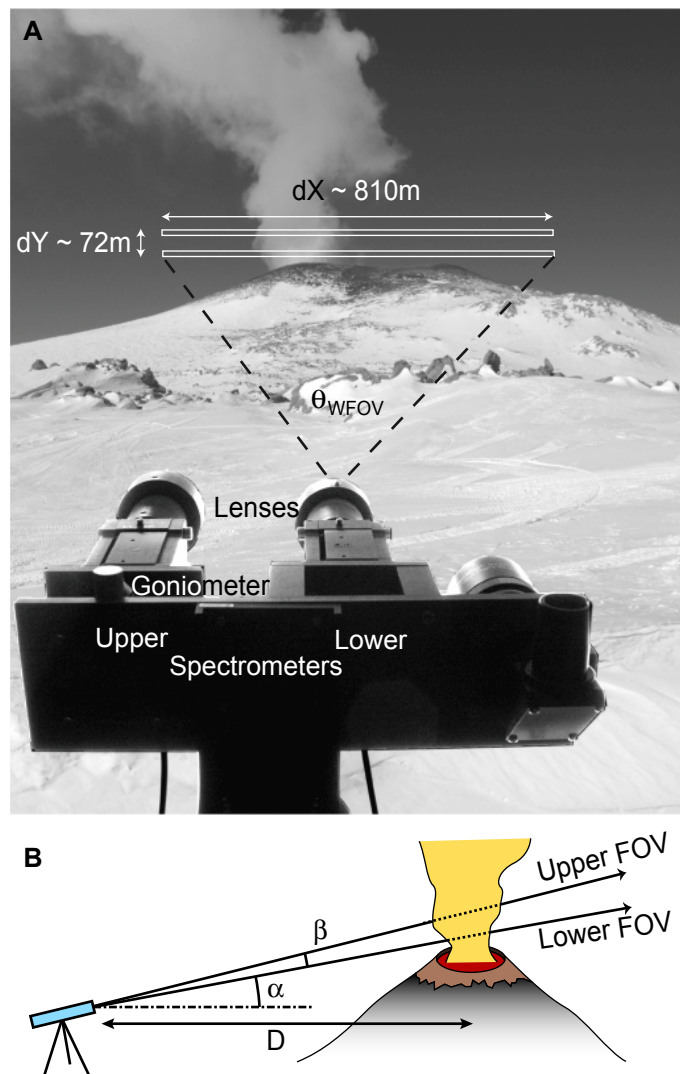


Figure 1: a) Photograph of Erebus volcano from Lower Erebus Hut showing a buoyant plume. Rectangles illustrate the wide fields of view of the two telescopes. Both are linked to UV spectrometers and the angle between the upper and lower fields of view is adjusted using a goniometer. b) Sketch of the geometry of the experiment with symbols used in text.

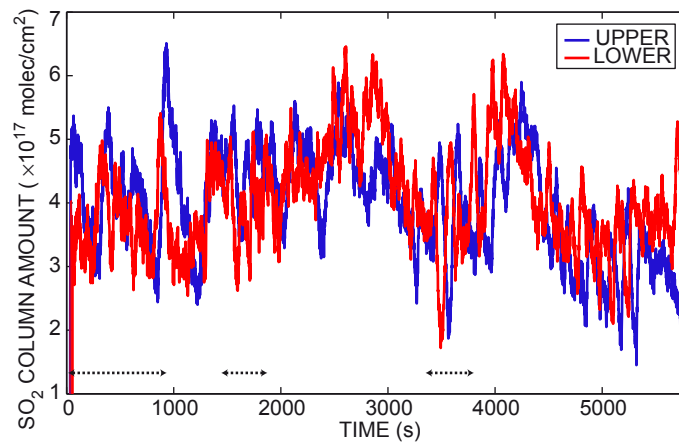


Figure 2: Time-series of SO_2 column amounts for both upper (blue) and lower (red) wide field of view spectrometers at Erebus on 26 December 2006 from $\sim 20:24$ h to $22:02$ h *UTC*. Dashed lines show periods of time when a bend was observable in the plume at a height less than 200 m above the crater, i.e., below the altitude of the upper spectrometer's FOV.

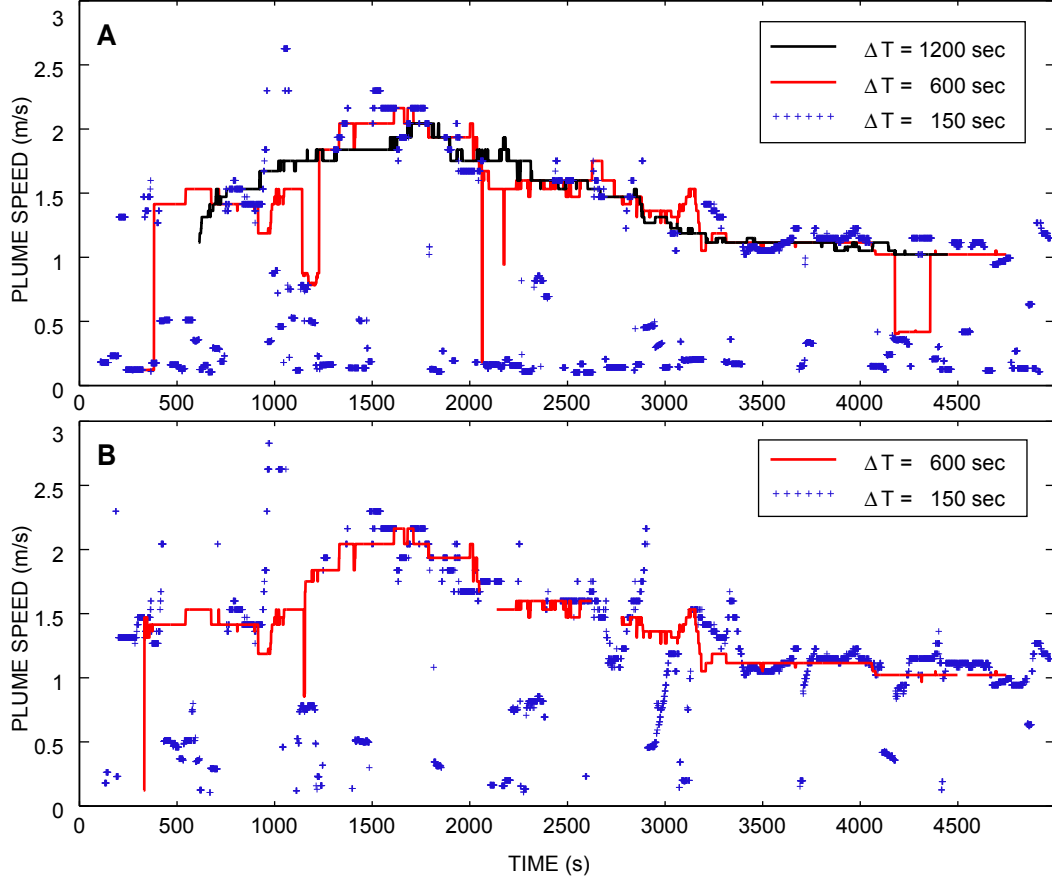


Figure 3: Plume speed *vs.* time since start of the dataset start at 20:24:48 UTC for (a) different sliding windows used for correlation analysis (with a duration ΔT of respectively 1200, 600 and 150 s), (b) a narrow and long sliding window ($\Delta T = 150$ and 600 s), using the criterion selecting the first local maximum in the CCF function, relative to the time shift, with an amplitude above a threshold of 0.5.

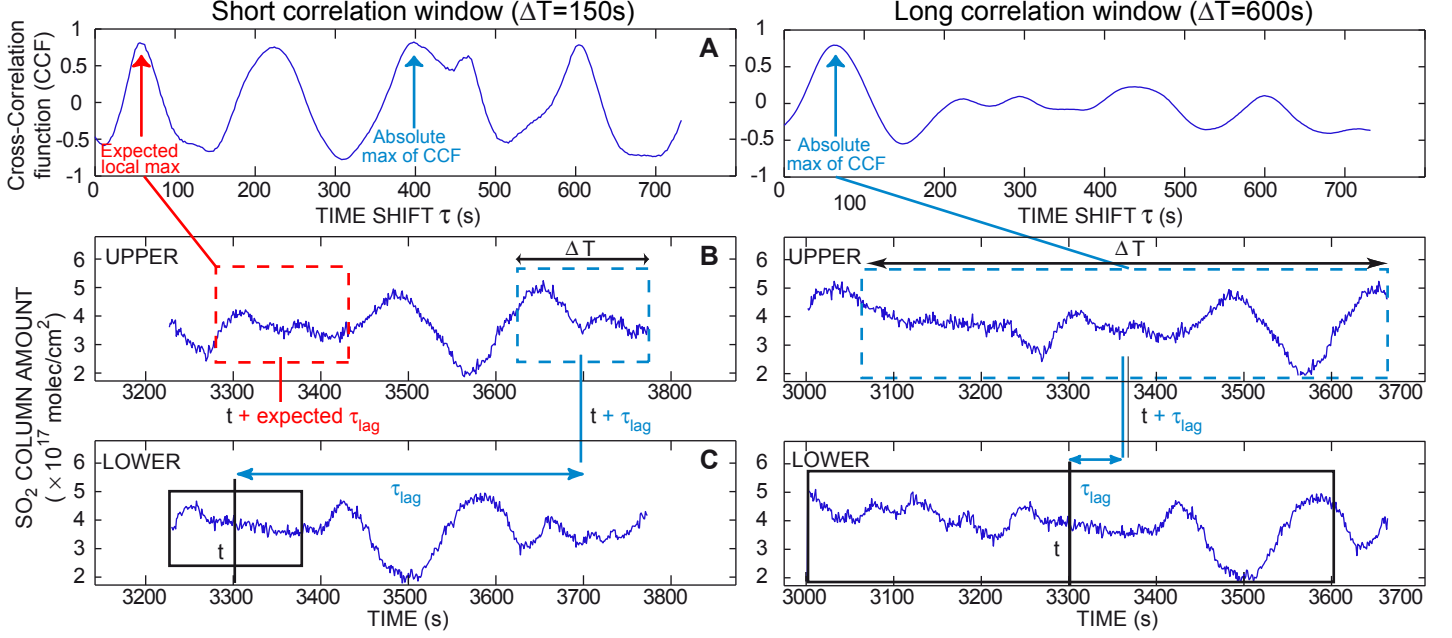


Figure 4: Example of correlation analysis giving a meaningless speed by selecting the absolute maximum (blue) of the cross correlation function (CCF) and not the first local maximum (red). Indeed, using a narrow correlation window of duration $\Delta T = 150$ s (on left), the absolute maximum does not correspond to the translation to the second instrument's FOV of the structure inside the lower correlation window, which would give the expected time lag. Rather it matches this initial structure with the translated signal of a similar neighbouring structure. This artifact does not occur with a long window (on right, here $\Delta T = 600$ s) because secondary peaks of the CCF are strongly flattened. (a) Plot of the cross correlation function with the time shift τ of the upper spectrometer correlation window. (b) and (c) shows signals for, respectively, the upper and lower spectrometers, from $(t - \Delta T/2)$ up to $(t + \tau_{lag} + \Delta T/2)$, with τ_{lag} the obtained time lag. Dashed lines underline correlation windows, centred and fixed in t for the lower spectrometer signal, centred in $(t + \tau)$ for the upper spectrometer signal with τ increasing until the time lag is found.

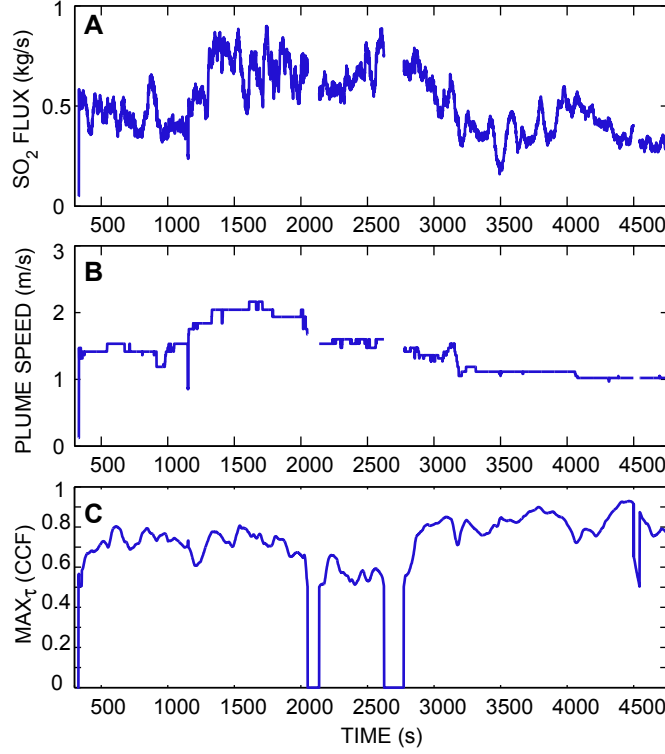


Figure 5: High time resolution (1 s) (a) SO₂ flux (in kg s⁻¹) from the lower spectrometer, (b) plume speed (in m s⁻¹), (c) cross correlation coefficient used for plume rise speed estimation fulfilling the two imposed criteria (i.e. corresponding to the first maximum of the cross correlation function with the time shift and which has to exceed a value of 0.5), *vs.* time from the data set start at 20:24:48 UTC on 26 December 2006, using a 10 min correlation window. Note that the cross correlation coefficient is artificially set to zero when it does not fulfil both required criteria. This results in four gaps in flux data during which speeds cannot be calculated from the correlation analysis.

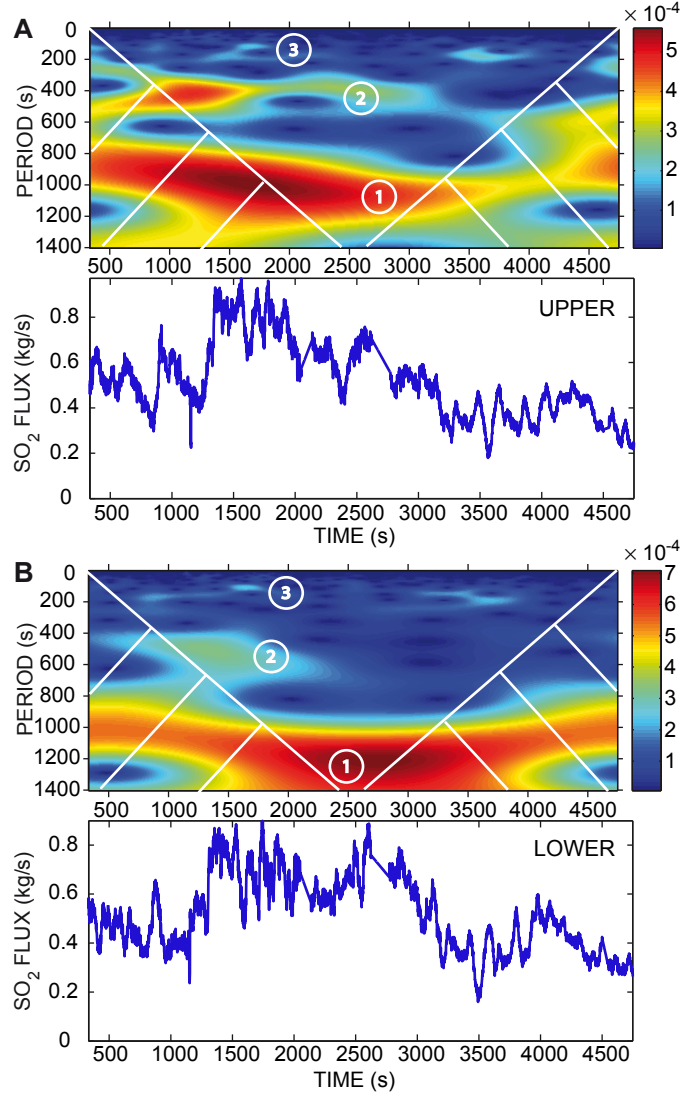


Figure 6: Wavelet transform (modulus) and time-series of SO₂ fluxes (in kg s⁻¹) for (a) upper and (b) lower spectrometers. Note that flux time-series are linearly interpolated to fill the few data gaps described in Fig. 5. The three populations of distinctive periods present in the signal (referenced as Patterns 1,2,3 in the figure) are discussed in the text. The cone of influence (white lines) delimits cross-hatched regions, inside which edge effects are non-negligible.

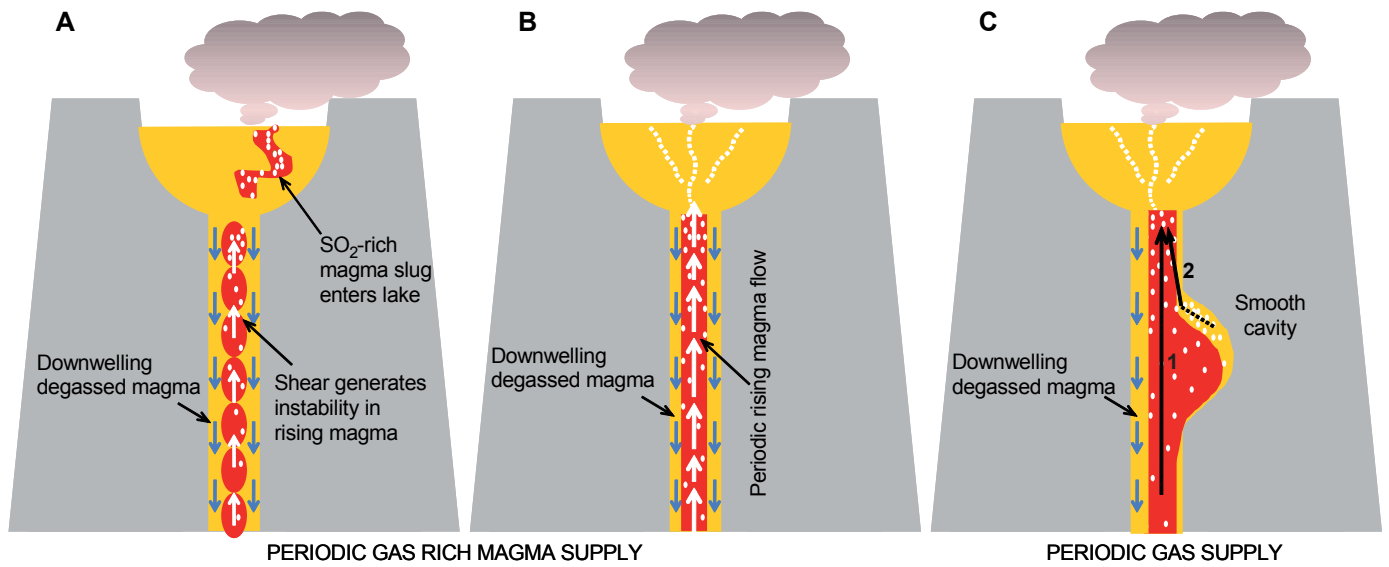


Figure 7: Cartoon illustrating different processes that can explain periodic degassing. (a) Periodic magma supply to the lava lake as a consequence of boudinage of the ascending magma flow, resulting from shear stresses between the buoyant gas-rich hot rising magma and downwelling cooler degassed counterpart (modified from (Oppenheimer et al., 2009b)); (b) periodic rising magma flow resulting from volatile-dependent viscosity; and (c) periodic gas supply to the lava lake arising from gas segregation in smooth cavities in the conduit.

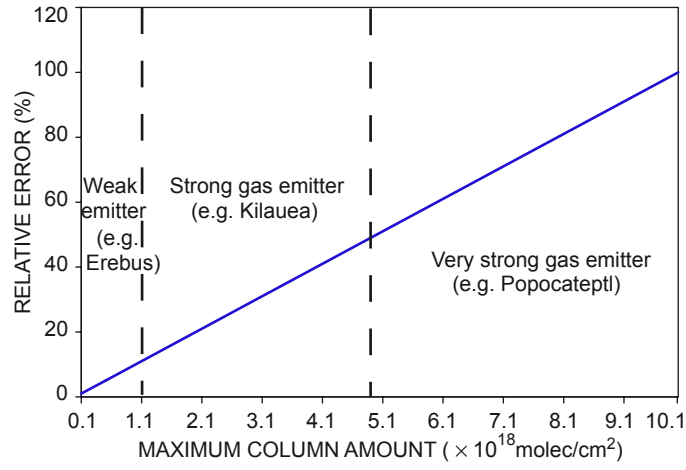


Figure 8: Relative error on the approximation of the mean SO_2 column amount (\overline{CA}) along the different directions in the wide field of view by the SO_2 column amount measured with the DW-FOV DOAS (CA_{WFOV}), according to Eq. A.18 (for more explanations, see Appendix A). For calculations, an averaged value of the SO_2 cross section, estimated over the wavelength range used for fit, is considered (10^{-19} cm²).